

# Single-shot autocorrelator for extreme-ultraviolet radiation

G. Kolliopoulos,<sup>1,2</sup> P. Tzallas,<sup>1</sup> B. Bergues,<sup>3</sup> P. A. Carpegiani,<sup>1,2</sup> P. Heissler,<sup>3</sup> H. Schröder,<sup>3</sup> L. Veisz,<sup>3</sup> D. Charalambidis,<sup>1,2</sup> and G. D. Tsakiris<sup>3,\*</sup>

<sup>1</sup>*Institute of Electronic Structure and Laser, FORTH, GR-71110 Heraklion (Crete), Greece*

<sup>2</sup>*Department of Physics, University of Crete, P.O. Box 2208, GR-71003 Heraklion (Crete), Greece*

<sup>3</sup>*Max-Planck-Institut für Quantenoptik, D-85748 Garching, Germany*

\*Corresponding author: [george.tsakiris@mpq.mpg.de](mailto:george.tsakiris@mpq.mpg.de)

Received September 27, 2013; revised January 14, 2014; accepted February 27, 2014;  
posted March 3, 2014 (Doc. ID 198478); published April 2, 2014

A novel single-shot second-order autocorrelation scheme for extreme-ultraviolet radiation (XUV) is proposed. It is based on an ion-imaging technique, which provides spatial information of ionization products in the focal volume of the XUV beam. Using simple analytical and detailed numerical modeling, an evaluation toward selecting an optimum configuration has been performed. The implementation of the concept to characterize attosecond pulses is discussed, and the proposed setups are assessed. © 2014 Optical Society of America

*OCIS codes:* (320.7100) Ultrafast measurements; (040.1880) Detection; (050.1960) Diffraction theory; (190.2620) Harmonic generation and mixing; (190.4180) Multiphoton processes; (260.7120) Ultrafast phenomena.

<http://dx.doi.org/10.1364/JOSAB.31.000926>

## 1. INTRODUCTION

The availability of attosecond pulses is now rather common in a number of laboratories. Spurred by rapid progress in modern laser systems, different methods of generation have been developed. They are all based on producing a quasi or pure spectral continuum in the XUV spectral range, which in the time domain corresponds to a train or even isolated attosecond pulses [1–3]. However, the readily accessible quantitative characterization of the attosecond pulse is still a challenge [4]. A complete measurement would provide information on the number of as-pulses produced, on their duration and ultimately about the temporal shape and spectral phase of the individual pulses. The common techniques used up to now can be divided into two main categories: (1) cross-correlation and (2) auto-correlation techniques. In the first category is the so-called RABITT (reconstruction of attosecond beating by interference of two-photon transitions) method for a train of attosecond pulses [5–8] and the “streaking” or the XFROG method for isolated pulses [9–12]. The second category includes the IVAC (intensity volume auto correlation) [13–16] and the XUV-FROG techniques [17,18]. All these methods have been frequently applied, but are in fact relatively cumbersome. They typically require acquisition over many (up to several millions) laser pulses and thus can only be utilized in conjunction with a high repetition rate laser or low repetition with good stability so that accumulation of single events is feasible.

For the various applications of the as-pulses envisioned, it is highly desirable to have a quick and reliable characterization of the attosecond source before launching an extensive experimental series. Furthermore, in case of poor laser parameter stability [pulse energy, carrier envelope phase (CEP), duration], it is important to be able to periodically optimize the as-pulse duration. This is of particular importance for

nonlinear applications of as-pulses [17,19–21]. Consequently, an approach in which a single-shot or at the most a few-shot measurement can reveal the necessary information in a routinely used fashion would be very helpful [22]. A technique for single-shot characterization of attosecond pulses based on spectral phase interferometry is the XUV SPIDER [23,24]. In this scheme, the two interfering beams are produced by splitting and manipulating the IR beam, which is used to generate the XUV photons. Although this characterization method is under certain conditions appropriate for XUV sources using atomic media, it is not in general applicable to every XUV source.

In this report, we propose a scheme in which the conventional method commonly used in fs-pulse metrology of the single-shot second-order intensity autocorrelation technique is extended by appropriate modifications to operation in the XUV spectral range. In the visible and IR part of the spectrum, the technique consists of crossing two pulses in a nonlinear crystal and measuring the second-harmonic light beam produced when the temporal delay between the two initial pulses is varied [25–28]. As no crystals are available for the wavelength range of the harmonic emission (10–80 nm), a replacement has to be found that will produce a two-photon signal. The second-order nonlinearity is a necessary condition to deduce the as-pulse duration. As it has been demonstrated in the first autocorrelation experiment of as-pulse trains [14], the two-photon ionization process in gas is an appropriate alternative for this purpose [29]. In the case of laser pulse, the region of the spatial overlap between the pulses is straightforward to image using an optical system from which the sought-after information on the pulse duration can be extracted. In the scheme we propose, the corresponding signal that needs to be recorded with spatial resolution stems from the ions

produced by two-photon ionization in the overlap region. The practicability of such a scheme has been demonstrated by Schultze *et al.* [30], who used an ion microscope to retrieve the spatial distribution of ions generated in the laser focus via ionization of a target gas. In their study, the authors demonstrated a magnification of 100 for a field-of-view of  $200 \times 100 \mu\text{m}$  and a spatial resolution better than  $4 \mu\text{m}$ . It should be emphasized that the resolution reported in [30] is the resolution of the particular experiments presented by the authors and does by no means represent an intrinsic limitation of the ion-microscope resolution, which can, in principle, reach a submicrometer level. The reported  $4 \mu\text{m}$  resolution rather results from the fact that the ion distribution shown in [30] was integrated over many laser shots and thus affected by beam-pointing fluctuations. Such beam-pointing fluctuations, however, would play no role in the single-shot autocorrelation scheme presented here. Furthermore, by adjusting the appropriate voltages in the ion optic section, the field-of-view of the instrument and the corresponding spatial resolution can be optimized to meet the requirements of a specific measurement.

Although the proposed scheme requires high XUV pulse energies to produce an analyzable signal, it has in principle the great advantage of deducing the most pertinent information in a single shot. This makes it more suitable for use with sources delivering intense XUV fluxes such as the XFEL or harmonic emission from gas or solid targets in which terawatt (TW) laser systems and high conversion efficiency schemes are employed.

The outline of this report is as follows: The concept on which the approach is based is explained in Section 2. To elucidate the basic idea, a simple analytical model is presented in Section 3 where the principle of operation is illustrated and the main conclusions are derived. Section 4 discusses setup optimization. The procedure of evaluating the diffraction integral in the general case of a group of harmonics and for

various intensity distributions is described in Section 4.A. The assessment of the arrangements investigated and a guide for the proper parameter selection are given in Sections 5.A and 5.B. Finally, a brief account of the ionization signal expected is given in Section 5.C.

## 2. CONCEPT

The method relies on the same principle employed in single-shot auto-correlation (SSAC) of pulses produced by lasers in the picosecond and subpicosecond time domains. The basic idea is to transform the temporal shape of the pulse into a spatial profile, which can be readily recorded and analyzed. The main differences here are that the setup has to be appropriate to handle XUV radiation and also capable of discerning a train of pulses. Therefore, the nonlinear crystal should be replaced by an atomic gas where two-photon ionization processes can take place and the ionization products must be recorded in two dimensions. Analogous to all-optical setups, we assume that two noncollinear XUV beams comprising a group of harmonics of the fundamental laser frequency cross each other in the plume of a gas jet. For illustration, we assume that the two beams are replicas of each other and emanate from two small openings at a distance  $d$  on the surface of a spherical mirror having focal length  $f$  (see Fig. 1). Assuming that the harmonics in the group are in phase, the temporal profile of the XUV pulse will generally have strong modulations and form a train of sub-laser-cycle duration pulses. In space, this translates to narrow regions where the electric field is confined, as illustrated in Fig. 1. The regions where the attosecond pulses of the train cross each other will propagate through the gas jet volume as long as the two XUV pulses overlap both spatially and temporally. A detector with imaging capabilities looking at the interaction region along a line of sight perpendicular to the plane defined by the two openings and the focus will record a series of lines parallel to the  $z$  axis.

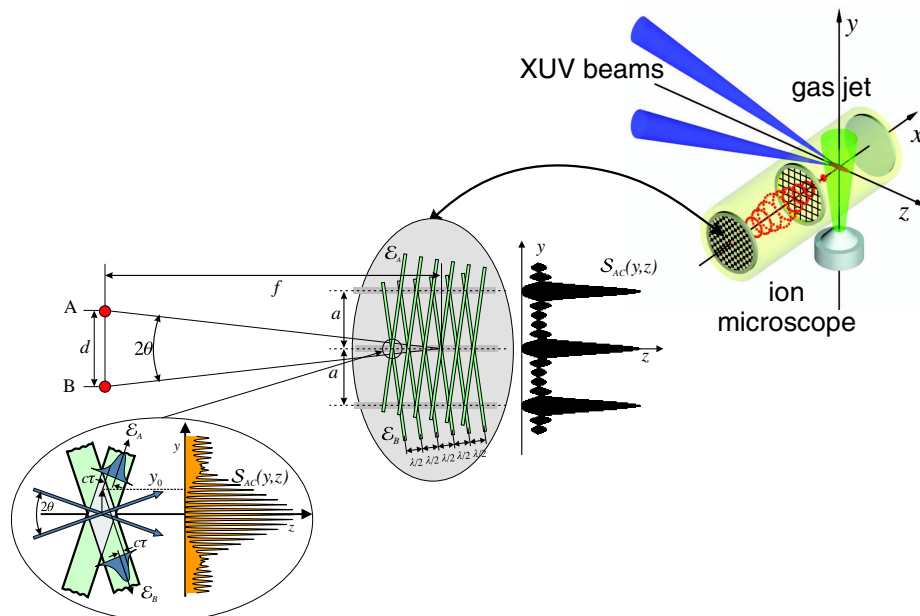


Fig. 1. Concept of the proposed SSAC scheme. In the upper-right inset, a schematic of the proposed setup is shown. The imaging ion-microscope provides an image of the ionization products around the common focal spots of the intersecting XUV beams. In the lower-left inset, the analogy to single-shot AC using fs-laser pulses and crystals is indicated. Provided that a two-photon ionization occurs, the fringe pattern shown schematically is the second-order AC trace to be analyzed.

Simple geometrical considerations lead to an expression for the distance  $a$  between these lines as

$$a = \frac{\lambda_0}{4 \sin \theta}, \quad (1)$$

where  $\theta = \arctan[d/(2f)]$  and  $\lambda_0$  the wavelength of the fundamental laser frequency. In deriving this expression, it was assumed that the harmonic emission emanates from an atomic medium. In this case only the odd harmonics are generated and as a consequence the subcycle pulses appear twice in every cycle of the fundamental frequency. For the plasma medium, the distance between the subcycle pulses would be  $\lambda_0$  [31].

Let  $N_{\text{ions}}$  be the number of ions produced at the point  $x, y, z$  of the interaction region where the two incident pulses coincide both spatially and temporarily. If the ionization process of the gas atoms is occurring via two-photon transitions,  $N_{\text{ions}}$  is proportional to the square of the instantaneous total intensity  $\mathcal{I}_{\text{tot}}^2(x, y, z, t) = |\mathcal{E}_A(x, y, z, t) + \mathcal{E}_B(x, y, z, t)|^4 = |\mathcal{E}_{\text{tot}}(x, y, z, t)|^4$  prevailing at this point. Here  $\mathcal{E}_A$  and  $\mathcal{E}_B$  are the amplitudes of the interfering fields from the two sources on the spherical mirror. To obtain the auto-correlation signal from the number of ions produced, we follow the same intuitive picture presented in [28], in conjunction with the second-harmonic generation in a nonlinear crystal. This is depicted in the lower-left inset of Fig. 1. For the present discussion, we assume that the two incident pulses have planar wavefronts and the gas density is spatially uniform. At each crossing of the subcycle pulses, the instantaneous number of ions  $N_{\text{ions}} \propto \mathcal{I}_{\text{tot}}^2 = |\mathcal{E}_A(t - \tau) + \mathcal{E}_B(t + \tau)|^4$  at a distance  $y_0$  from its bisector depends on the delay between two different parts of the overlapping pulses (see lower-left inset in Fig. 1). The delay  $\tau$  is related to the physical distance  $y_0$  by  $\tau = y_0 \sin \theta / c$  where  $c$  is the velocity of light in the medium. The ion signal integrated over the XUV pulse width is proportional to the interferometric autocorrelation function  $\mathcal{S}_{\text{AC}}$  of the incident pulse:

$$\mathcal{S}_{\text{AC}}(x, y, z) \propto \int_{-\infty}^{+\infty} |\mathcal{E}_A(t - \tau) + \mathcal{E}_B(t + \tau)|^4 dt. \quad (2)$$

A spatially resolved ion signal of the interaction region with sufficient resolution reveals the most pertinent information about the XUV pulse in a single event. For example, provided the field-of-view encompasses the whole interference pattern, the number of attosecond pulses can be immediately deduced. Furthermore, all the information from an interferometric AC trace in the case of visible wavelengths is also available here; most importantly an estimate of the duration and possibly of the chirp of the generated attosecond pulses. Namely, if the spatial width of the fringe-averaged signal in the overlapping regions shown in Fig. 1 is  $\Delta y = c \cdot \tau_{\text{AC}}$ , then the duration of the attosecond pulse would be

$$\tau_{\text{as}} = \tau_{\text{AC}} \cdot \sin \theta. \quad (3)$$

There is, nevertheless, a fundamental difference between this AC scheme and that employed in the visible range using crystals. Because of momentum conservation, the second-harmonic emission that is generated using crystals is produced along the bisector (observation) direction only in the regions where the beams cross each other in temporal

coincidence inside the crystal, i.e., each beam by itself does not produce any signal in this direction. This gives the possibility of measuring the background-free single-shot AC signal. In the case of two-photon ionization, a signal is produced wherever sufficient intensity is available and therefore also in regions where only one beam is present. The background signal is indicated in Fig. 1, and it will be quantified for specific cases in Section 3.

### 3. MODEL CALCULATION

In this section, a simplified model is used to analytically investigate the main features of the interferometric auto-correlation function given in Eq. (2). Two XUV beams consisting of  $N$  harmonics of the fundamental laser frequency  $\omega_0$  are assumed, each emanating from an aperture of diameter  $D$  on a spherical surface with focal length  $f$ . Due to focusing of the spherical mirror, they interfere within an angle  $\theta$  at the focus (see Fig. 2). To make the calculation tractable, first two plane waves are considered interfering at the focus of the spherical surface. The effect of focusing is taken into consideration in an ad hoc manner in the second step.

Given the difference in the propagation vectors of the two plane waves indicated in Fig. 2, the combined field due to the  $q$ th harmonic from the two sources  $\mathcal{E}_q(y, z, t)$  at the  $y - z$  plane is

$$\begin{aligned} \mathcal{E}_q(y, z, t) &= E_q [e^{j(l_q y + k_q z - \omega_q t)} + e^{j(-l_q y + k_q z - \omega_q t)}] \\ &= E_q [e^{j(k_q z - \omega_q t)} (e^{+j l_q y} + e^{-j l_q y})] \\ &= 2E_q \cos(l_q y) e^{j(k_q z - \omega_q t)}, \end{aligned} \quad (4)$$

where  $E_q$  is the amplitude of the  $q$ th harmonic,  $k_q = q(2\pi/\lambda_0) \cos \theta$ ,  $l_q = q(2\pi/\lambda_0) \sin \theta$ ,  $\omega_q = q\omega_0$  and  $\lambda_0$  is the fundamental wavelength. In the expression in Eq. (4), the time delay  $\tau$  between the two beams is indirectly included by the geometry via the dependence on the coordinate  $y$ . The total instantaneous intensity  $\mathcal{I}_{\text{tot}}(y, z, t)$  at the region where there is complete overlap will be

$$\begin{aligned} \mathcal{I}_{\text{tot}}(y, z, t) &= \sum_q \mathcal{E}_q(y, z, t) \times \sum_p \mathcal{E}_p^*(y, z, t) \\ &= \sum_q 2E_q \cos(l_q y) e^{j(k_q z - \omega_q t)} \\ &\quad \times \sum_p 2E_p \cos(l_p y) e^{-j(k_p z - \omega_p t)} \\ &= 4 \sum_{q,p} E_q E_p \cos(l_q y) \cos(l_p y) e^{j[(k_q - k_p)z - (\omega_q - \omega_p)t]}. \end{aligned} \quad (5)$$

The first-order AC signal is proportional to the time-average intensity, i.e., to  $\hat{\mathcal{I}}_{\text{tot}}(y, z) \propto \int_t^{t+T_0} \mathcal{I}_{\text{tot}}(y, z, t) dt$  with  $T_0$  the period of the fundamental wave. It is easily seen that terms containing the integral  $\int e^{\pm j(q-p)\omega_0 t} dt$  will average to zero unless  $q = p$ . Retaining only the surviving terms, one obtains

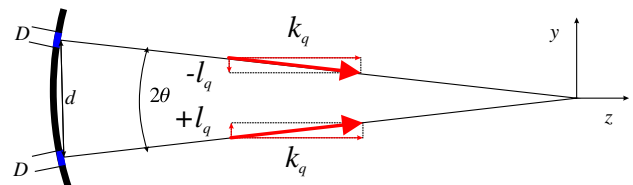


Fig. 2. Geometry considered in the model calculation.

$$\begin{aligned}\hat{\mathcal{I}}_{\text{tot}}(y) &= 4 \sum_q E_q^2 \cos^2(l_q y) \\ &= 4 \sum_q E_q^2 \cos^2\left(q \frac{\pi y}{2a}\right).\end{aligned}\quad (6)$$

As expected, the time-average intensity pattern becomes independent of  $z$ . This justifies the picture presented in Fig. 1, i.e., in a 2D ion image of the interaction region by a time integrating detector, the lines along which the crossing points of the attosecond pulses propagate would appear as stripes.

The second-order AC signal is proportional to the average value of the square of the time dependent intensity. Therefore, the intensity should be squared before the time average value is calculated, i.e., one should start from the following expression:

$$\begin{aligned}\mathcal{I}_{\text{tot}}^2(y, z, t) &= \left[ \sum_q 2E_q \cos(l_q y) e^{j(k_q z - \omega_q t)} \times \sum_p 2E_p \cos(l_p y) e^{-j(k_p z - \omega_p t)} \right]^2 \\ &= 2^4 \left[ \sum_{q,p} E_q E_p \cos(l_q y) \cos(l_p y) e^{j[(k_q - k_p)z - (\omega_q - \omega_p)t]} \right]^2 \\ &= 2^4 \sum_{q,p,n,m} E_q E_p E_n E_m \cos(l_q y) \cos(l_p y) \cos(l_n y) \cos(l_m y) \\ &\quad \times e^{j[(k_q - k_p + k_n - k_m)z - (\omega_q - \omega_p + \omega_n - \omega_m)t]}.\end{aligned}\quad (7)$$

Using the multiple sum in the last expression of Eq. (7), the time average of each term can be calculated. Again taking into consideration that terms now containing the integral  $\int e^{\pm j(q-p+n-m)\omega_0 t} dt$  will average to zero unless  $q-p+n-m=0$ , one obtains for the second-order AC signal as

$$\begin{aligned}\hat{\mathcal{I}}_{\text{tot}}^2(y) &= 2^4 \sum_{q,p,n,m} \mathcal{R}_{q,p,n,m} E_q E_p E_n E_m \cos(l_q y) \cos(l_p y) \cos(l_n y) \cos(l_m y) \\ &= 2^4 \sum_{q,p,n,m} \mathcal{R}_{q,p,n,m} E_q E_p E_n E_m \cos\left(q \frac{\pi y}{2a}\right) \cos\left(p \frac{\pi y}{2a}\right) \\ &\quad \times \cos\left(n \frac{\pi y}{2a}\right) \cos\left(m \frac{\pi y}{2a}\right) \\ &\text{where } \mathcal{R}_{q,p,n,m} = 1 \text{ for } q+p-n-m=0 \text{ and} \\ &\mathcal{R}_{q,p,n,m} = 0 \text{ otherwise.}\end{aligned}\quad (8)$$

The factor  $\mathcal{R}_{q,p,n,m}$  is introduced to take into consideration the effect of time averaging. It is interesting to note that the last result is not obtained by simply squaring the time average intensity in Eq. (6).

To illustrate the behavior of the interference pattern and the form of the first and second AC trace, we consider a specific example. For a group of odd harmonics in the range  $q_a = 101$  to  $q_b = 111$  and for  $f = 5$  cm,  $d = 0.3$  cm and  $\lambda = 800$  nm the last expressions in Eqs. (6) and (8) are plotted in Fig. 3. For these parameters, the distance between the crossings of the attosecond pulses is  $a \simeq 6.7 \mu\text{m}$ . It is seen that while the first-order AC is symmetric around an average value, the second-order AC exhibits the typical auto-correlation behavior with a signal-to-background ratio of 8:1 as in the case of single frequency interferometric AC. The fine structure inside each peak is due to the interference of the individual harmonics. It

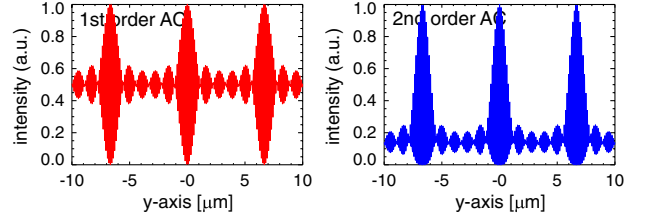


Fig. 3. Plot of the expression in Eqs. (6) and (8) for a group of equal amplitude odd harmonics between  $q = 101 \dots 111$  and for  $f = 5$  cm,  $d = 0.3$  cm, and  $\lambda = 800$  nm.

is to be noted here that the choice of the specific group of harmonics (H101–H111) is judicial to better demonstrate the features of multifrequency AC traces. In the following sections, a more realistic case of lower harmonics in the range H9–H15 is considered.

Up to now the diffraction due to the apertures on the mask has not been taken into account. We now assume uniform illumination over the area of the opening having radius  $R = D/2$ . As each source is located on the surface of a focusing mirror, the focal spot will then be an Airy pattern. For waves having a wavelength  $\lambda_0$ , the pattern at the focal plane is (see [32])

$$\mathcal{I}(y) = \left[ \frac{2J_1(v)}{v} \right]^2, \quad (9)$$

where  $v = (2\pi/\lambda_0)(R/f)r$  with  $r = \sqrt{(x^2 + y^2)}$ . Thus the time-average intensity for a group of harmonics in Eq. (6) is modified as follows:

$$\hat{\mathcal{I}}_{\text{tot}}(y) = 4 \sum_q \left[ E_q \frac{2J_1(v_q)}{v_q} \cos(u_q) \right]^2, \quad (10)$$

where  $u_q = q(2\pi/\lambda_0)y \sin \theta = q(\pi/2)(y/a)$  and  $v_q = q(2\pi/\lambda_0)(R/f)r$ . Similarly, the second-order AC signal in Eq. (8) becomes

$$\begin{aligned}\hat{\mathcal{I}}_{\text{tot}}^2(y) &= 2^8 \sum_{q,p,n,m} \mathcal{R}_{q,p,n,m} E_q E_p E_n E_m \\ &\quad \times \frac{J_1(v_q)}{v_q} \cos(u_q) \frac{J_1(v_p)}{v_p} \cos(u_p) \frac{J_1(v_n)}{v_n} \\ &\quad \times \cos(u_n) \frac{J_1(v_m)}{v_m} \cos(u_m)\end{aligned}$$

$$\begin{aligned}\text{where } \mathcal{R}_{q,p,n,m} &= 1 \text{ for } q+p-n-m=0 \text{ and} \\ \mathcal{R}_{q,p,n,m} &= 0 \text{ otherwise.}\end{aligned}\quad (11)$$

The last expressions in Eqs. (10) and (11) for  $D = 100 \mu\text{m}$  are plotted in Fig. 4 for the same geometrical parameters as in

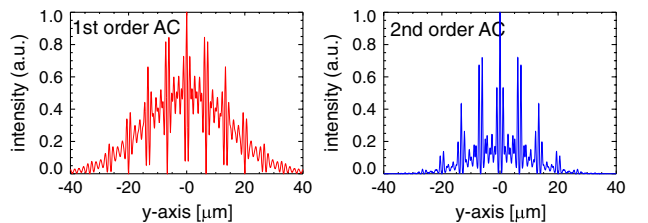


Fig. 4. Plot of the expression in Eqs. (10) and (11) for  $q = 9 \dots 15$  and equal amplitudes. The geometry parameters are the same as in Fig. 3.

the previous example, yet with group harmonics of  $q = 9 \dots 15$ . This harmonic selection is technically feasible and ensures two-photon ionization in conjunction with He atoms [14,16]. The fine structure seen in Fig. 4 is due to interference of the light from the two apertures while the overall shape is determined by diffraction through a single aperture (Airy pattern). Thus the signal area is limited by the Airy spot size resulting at the focus of the spherical mirror and is given by  $R_{\text{Airy}} \approx 1.22f\lambda_{q_0}/D \simeq 54.2 \mu\text{m}$  with  $q_0$  the lowest harmonic in the selection. In order to be able to deduce, e.g., whether a single attosecond pulse is produced or not, at least three sub-cycle peaks should fit in the observable area. This imposes the condition  $R_{\text{Airy}} \geq a$ . The smaller the diameter  $D$  of the apertures, the larger the Airy radius. This, however, drastically reduces the XUV intensity at the focus. Alternatively, one can increase the distance  $d$  of the two apertures to obtain shorter distance  $a$  between the peaks. The drawback then is that a higher spatial resolution is required to adequately resolve the peaks. As a consequence for optimum operation, a compromise in the selection of the apertures diameter and their distance should be carefully made (see discussion in Section 5).

#### 4. SETUP OPTIMIZATION

In this section, we perform a detailed study to determine the optimum arrangement for the use of the SSAC device in conjunction with attosecond light sources. The objective is to determine the geometry as to achieve the maximum possible throughput and the best resolution. To be able to consider quite general but realistic cases, we apply the formulation presented in [32] for the diffraction integral at the focus of a spherical converging wave. We then consider various masks or geometries for the spherical mirror from where the converging wave emanates.

##### A. Calculation of the Diffraction Integral

The starting point is the expression given in [32] for the calculation of the 3D monochromatic light distribution near focus, namely,

$$U_{\text{tot}}(P) \propto \iint_W \frac{e^{jk_0(s-f)}}{s} dS, \quad (12)$$

where  $k_0 = (2\pi/\lambda_0)$  and  $\lambda_0$  the wavelength of the converging wave. The point  $Q$  with coordinates  $x_Q, y_Q, z_Q$  is located on the mirror surface  $W$ , and  $P$  is the observation point with coordinates  $x_P, y_P, z_P$ , both with respect to a system centered at the focus of the spherical wave. The distance  $s$  between the point  $Q$  and  $P$  determining the phase factor is derived from  $s^2 = (x_P - x_Q)^2 + (y_P - y_Q)^2 + (z_P - z_Q)^2$ . To apply the method to our case, one has to consider three notable differences:

1. The illumination from the spherical surface is restricted to two apertures through an appropriate mask.
2. The illumination is not monochromatic, i.e., there are contributions from a group of harmonics.
3. The time dependence cannot be factored out.

In this case, the diffraction integral has to be modified as follows:

$$U_{\text{tot}}(P, t) \propto \iint_W M(Q) \sum_q e^{j[k_q(s-f) - \omega_q t]} dS, \quad (13)$$

where now  $k_q = q(2\pi/\lambda_0)$  and  $\omega_q = q\omega_0$ ,  $M(Q)$  is the mask on the spherical surface and the sum runs over the harmonic numbers in the group.

If  $q = 1$ , i.e., monochromatic illumination, then the time-dependent factor can be taken out of the integral, and the time average intensity is simply  $\hat{\mathcal{I}}_{\text{tot}} \propto U_{\text{tot}} U_{\text{tot}}^*$ . In the case of a harmonic synthesis, the situation is more complicated. The different frequencies give rise to temporal beating (attosecond pulse train), and over a period the variation is not simply  $\propto \cos(\omega t)$ . For this reason, the evaluation of the time average intensity in case of a group of harmonics needs special attention. The diffraction integral in this case can be written as

$$U_{\text{tot}}(P, t) \propto \sum_q U_q e^{-j\omega_q t} \quad \text{where } U_q = \iint_W M(Q) e^{j[k_q(s-f)]} dS. \quad (14)$$

In analogy to Eq. (5), the corresponding instantaneous total intensity  $\mathcal{I}_{\text{tot}}(x, y, z, t)$  is given by

$$\begin{aligned} \mathcal{I}_{\text{tot}}(x, y, z, t) &\propto \sum_q U_q e^{-j\omega_q t} \times \sum_p U_p^* e^{+j\omega_p t} \\ &\propto \sum_{q,p} U_q U_p^* e^{-j(\omega_q - \omega_p)t}. \end{aligned} \quad (15)$$

The time average can now be calculated, and, using the same argument for the cross terms as in Eq. (5), one obtains

$$\hat{\mathcal{I}}_{\text{tot}}(x, y, z) \propto \sum_q U_q U_q^*. \quad (16)$$

The second-order AC signal will be proportional to

$$\begin{aligned} \mathcal{I}_{\text{tot}}^2(x, y, z, t) &\propto \left[ \sum_{q,p} U_q U_p^* e^{-j(\omega_q - \omega_p)t} \right]^2 \quad \text{and thus to} \\ \hat{\mathcal{I}}_{\text{tot}}^2(x, y, z) &\propto \sum_{q,p,n,m} \mathcal{R}_{q,p,n,m} [U_q U_p U_n^* U_m^*], \end{aligned}$$

where  $\mathcal{R}_{q,p,n,m} = 1$  for  $q + p - n - m = 0$  and  $\mathcal{R}_{q,p,n,m} = 0$  otherwise. (17)

In what follows, we apply these formulas to numerically calculate the second-order AC signal for various masks of practical interest.

##### B. Two-Aperture Mask

As a first example, we consider a mask in which two pinholes select a small portion of the XUV beam incident on a spherical mirror. The XUV profile is assumed to be Gaussian with a FWHM waist of  $2r_b = 3.0 \text{ mm}$  while the mask geometrical dimensions are the same as those considered for the analytical model in Section 3. The XUV profile and the mask are shown in Fig. 5 along with the patterns in two planes of the second-order AC trace. Comparing the line-out along the  $y$  axis of the focal plane pattern obtained through the numerical evaluation of the diffraction integral in Eq. (17), it is seen that is identical to the one from the analytical model shown in Fig. 4. This is to

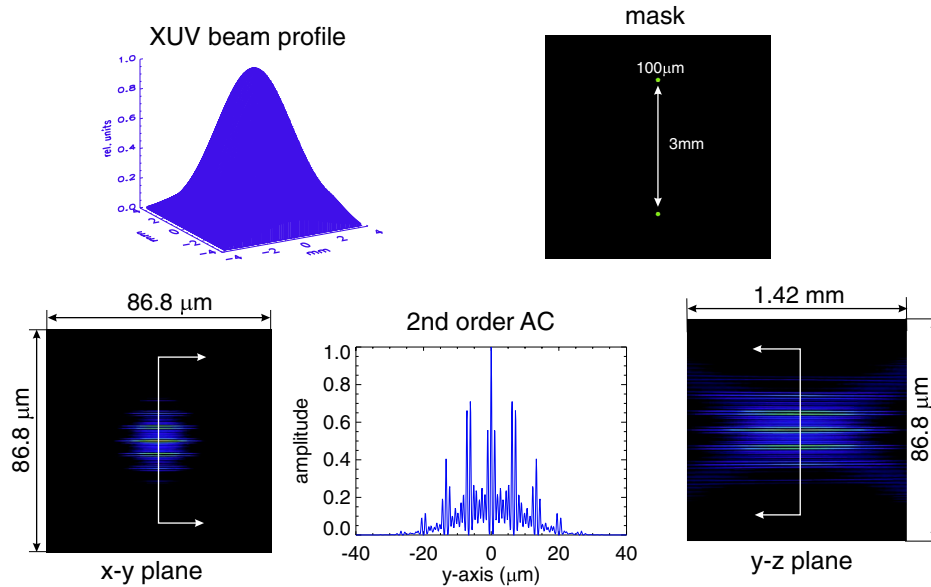


Fig. 5. Second-order AC pattern due to the interference of the harmonic radiation emanating from two apertures of  $100\ \mu\text{m}$  in diameter. Upper panels: The profile of the converging XUV beam and the mask imposed to it. Lower panels: The second-order AC pattern in the two planes around the XUV focus as obtained from the numerical evaluation of Eq. (17). The geometry parameters and the harmonic selection are the same as in Fig. 4 ( $q = 9\dots 15$  and equal amplitudes).

be expected since the intensity variation over the pinhole openings of the Gaussian beam and the focusing effect of the converging wave are negligible. The agreement constitutes a reliable confirmation for the validity and correctness of the numerical method based on the diffraction integral.

According to the basic concept of the SSAC device, the pattern in the  $y$ - $z$  plane shown in Fig. 5 contains the information that needs to be recorded. For the specific geometry considered, its relevant dimensions are quite accessible to measurements assuming a sub- $\mu\text{m}$  resolution capability of the ion microscope to be used. However, due to the large axial extent of the focus, the XUV intensity might not be high enough to

produce two-photon ionization. In addition, the two-aperture mask is inefficient, as it exploits a very small part of the incident XUV beam.

### C. Two-Slit Mask

An alternative setup in which a better use of the available XUV energy is made is the two-slit mask. In this configuration, instead of two pinholes, there are two slits with width equal to the diameter of the pinhole in the previous example but of length extending over the whole XUV beam profile. This mask is shown in Fig. 6. The effect is that the focal pattern in the  $y$ - $z$  plane and  $x$ - $y$  plane has much smaller extent in the  $x$  and  $z$

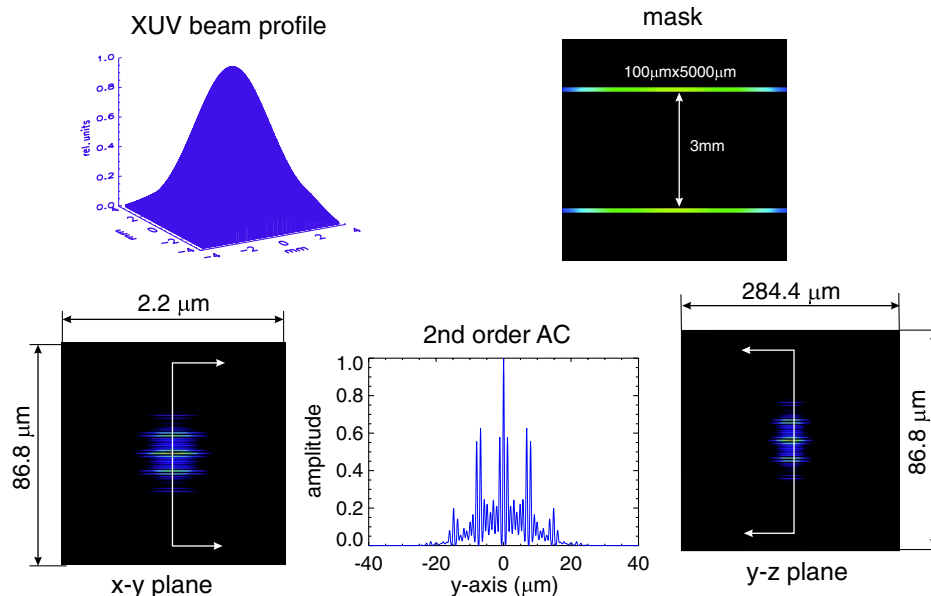


Fig. 6. Second-order AC pattern due to the interference of the harmonic radiation emanating from two slits of  $100\ \mu\text{m}$  wide and  $5\ \text{mm}$  long. Upper panels: The profile of the converging XUV beam and the mask imposed to it. Lower panels: The second-order AC pattern in the two planes around the XUV focus as obtained from the numerical evaluation of Eq. (17). The geometry parameters and the harmonic selection are the same as in Fig. 4 ( $q = 9\dots 15$  and equal amplitudes).

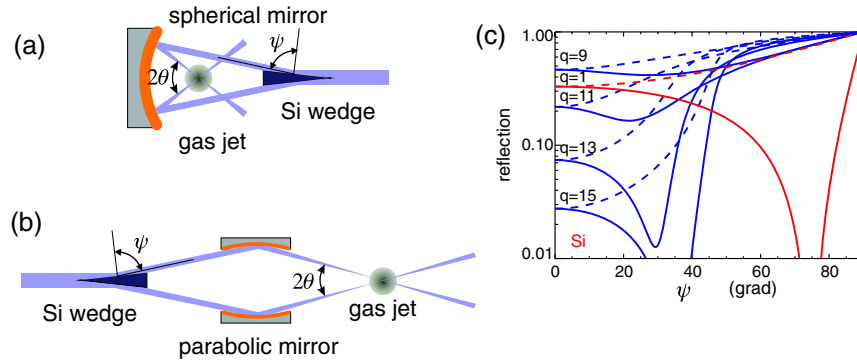


Fig. 7. Schematic diagrams of two possible setups for a cross-beam arrangement. (a) Setup for low-order harmonics (long wavelength XUV emission) and (b) for higher-order harmonics (short wavelength XUV emission). (c) Reflectivity of Si as a function of angle of incidence  $\psi$  for parallel (solid line) and perpendicular (dashed line) polarization and for the indicated harmonic orders  $q$ .

direction, but in the  $y$  direction remains the same. This is depicted in Fig. 6 where the second-order AC signal is shown as calculated for this mask using Eq. (17). As expected, the line-out of the signal along the  $y$  axis in this case is identical to the one from the previous one. An assessment of the factor gained in intensity using this mask is given in Section 5.A.

#### D. Beam Splitter

In the setups discussed in Sections 4.B and 4.C, it is obvious that in order to obtain an interaction region large enough to record sufficient information, the majority of the XUV energy is lost. This is primarily imposed by the requirement of dispersing the interference pattern to an extent that an ion microscope can “see” the details, i.e., the beats in the focus of the crossed beams. Still these setups are applicable if the XUV source to be characterized is intense enough and the recording ion microscope possesses adequate resolution.

In this section, we investigate an alternative setup that would be more appropriate for relatively weak XUV sources. It is based on the wavefront-splitting technique, and it is shown schematically in Fig. 7. As no conventional beam splitters exist for XUV radiation, the wavefront, instead of the amplitude of the beam, is divided into two. This can be easily achieved by using a wedge out of proper material as depicted in Fig. 7. For example, Si exhibits for the nearly grazing angle of incidence  $\psi$  very high reflectivity and for a wide spectral range [see Fig. 7(c)]. Furthermore, if the angle of incidence is chosen equal to the Brewster angle  $\theta_B(\text{Si}) \simeq 75^\circ$  for  $\lambda = 800$  nm and parallel polarization, the same component can be used to substantially suppress the fundamental laser frequency.

After splitting the beam into two, an optical arrangement can be used to cross and focus the two beams under a given angle  $\theta$  thus generating an interference pattern within a gas jet where the two-photon ionization takes place. We show two possible arrangements: one involving nearly perpendicular reflection and therefore limited to low-order harmonics [Fig. 7(a)] and another employing grazing incidence optics, which is more appropriate for high-order harmonics [Fig. 7(b)]. The first option imposes the condition  $\theta \geq \pi - 2\psi$  while the second has the advantage of independently choosing  $\theta$  and  $\psi$  but is more demanding in bringing the focus of the two beams to coincidence. These schemes have the advantage that the total XUV energy after reflection off a wedge is focused in the gas medium. The main drawbacks are the

reflection losses on the wedge and the small focus due to large illumination aperture.

For reasons of comparison, we use the same experimental parameters as in the previous examples, i.e., the same group of harmonics  $q = 9 \dots 15$  of equal amplitudes) and Gaussian XUV beam with a FWHM waist of  $2r_b = 3.0$  mm. This corresponds to an  $1/e^2$  waist of  $w_b = \sqrt{2/\ln 2} r_b = 2.5$  mm. The beam, however, is divided into two equal portions, which subsequently are focused by a single optical component and cross each other at their focus. Since in this configuration the illuminated aperture is much larger compared to the previous cases, the condition  $R_{\text{Airy}} \geq a$  necessary to observe more than one attosecond beat at the focus is not satisfied for the same focal length. To compensate for this, the focal length of the spherical mirror must be increased. We choose  $f = 100$  cm and an angle  $\theta = 2^\circ$ . In this case,  $a = 5.7 \mu\text{m}$  and  $d = 70$  mm. The focal extent along the  $y$  direction is estimated from  $w_{0,y} \approx f \lambda_q / (\pi w'_b) \simeq 22.2 \mu\text{m}$  with  $w'_b = w_b/2$ . Here we consider the focal extent of the  $q = 9$  harmonic, i.e., of the longest wavelength, and we take the waist of the half beam to be approximately half of the original waist. Accordingly, the focal extent in the  $x$  direction is  $w_{0,x} \approx f \lambda_q / (\pi w_b) \simeq 11.1 \mu\text{m}$ . The results of the numerical integration of the diffraction integral in Eq. (17) are shown in Fig. 8. It is seen that the estimates of the focal extent agree very well with the results of the calculation. For the chosen experimental parameters, a readily resolved pattern comprising at least three attosecond beats is produced. The spatial extent (FWHM) of the central peak is  $\Delta y \approx 2 \mu\text{m}$ , which corresponds to  $\tau_{\text{as}} = \sin \theta \cdot \Delta y / c \simeq 230$  as, which is indeed the duration of the individual attosecond pulses in the train formed by the H9–H15 harmonics if they are phase locked and of equal amplitude.

A variation of the beam-splitter method is the use of a split mirror in which the two parts are tilted with respect to the propagation axis. This way a magnified interference pattern is obtained just before the focus. The disadvantage of this setup is that, for realistic conditions, the region to be recorded is located close to the foci of the two half-beams. This would make the weak signal of the AC pattern difficult to distinguish from the signal due to the high intensity prevailing at the foci of the two half-beams.

#### 5. SETUP ASSESSMENT

The criteria on which the most appropriate setup can be chosen depend mainly on two experimental parameters:

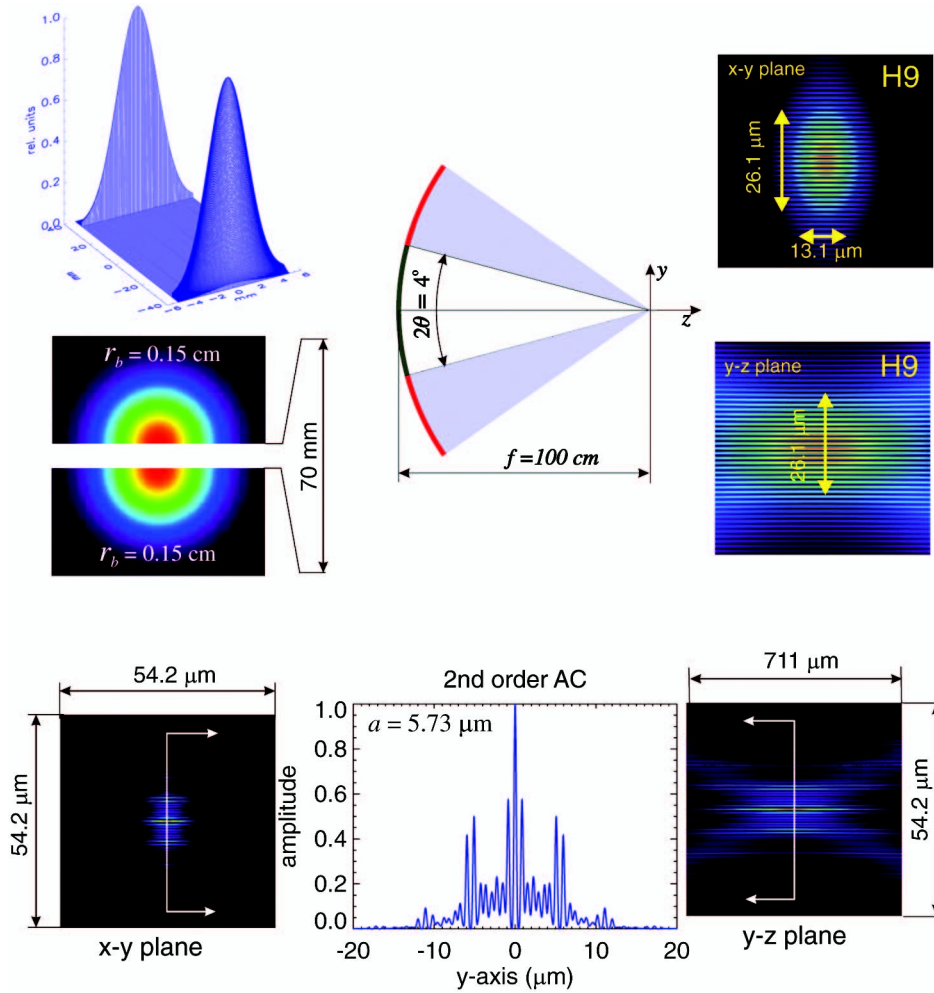


Fig. 8. Numerical calculation of the cross-beam arrangement using a wavefront beam splitter. The upper panel shows the illumination geometry and the interference pattern for the H9 harmonic at the focus. The FWHM extent of the focal spot in the two directions is also indicated. The lower panel shows the second-order signal due to two-photon ionization by the harmonic group of H9–H15. The pattern in the  $yz$  plane is what an ion microscope with enough resolution would record.

(1) the spatial resolution of the ion-microscope  $\Delta s$  and (2) the maximum XUV power  $\mathcal{P}_{\text{XUV}}$  available by the source. The given spatial resolution determines the minimum size of the interaction region required to discern enough details to extract the pertinent information. On the other hand, a larger interaction region means lower XUV intensity in which case the two-photon process rapidly becomes less efficient, and, as a result, the corresponding signal rapidly deteriorates. It becomes apparent that for the given values of these two parameters, one must carefully navigate through the remaining parameters such as type of mask or arrangement, spherical mirror focal length, and angle of intersection in order to obtain the most suitable setup. In what follows, we discuss the advantages and disadvantages of each of the setups we have considered and point out the interplay of the various parameters.

### A. Efficiency Comparison

Since the application envisaged is based on a two-photon process, it is of utmost importance to examine the efficiency of the overall setup so that an estimate of the achievable intensity can be made. Previous experiments [14,16,20] have shown that an XUV intensity of  $I_{\text{XUV}} \gtrsim 10^{11}$  W/cm<sup>2</sup> is needed

for recording a volume AC trace. In the scheme, we propose here the signal is not spatially integrated as in previous experiments, but a 2D image of the ionization products is required to deduce the sought-after information. This increases the minimum XUV intensity needed for recording an analyzable signal by at least a factor of 100. It is therefore essential to examine the efficiency of each arrangement we have considered. Here we compare, from the point of view of the mean intensity in the intersection volume, the three different implementations of this autocorrelation method we have discussed so far, i.e.,

1. Using a mask with two apertures of diameter  $D = 100.0$   $\mu\text{m}$  in a distance of  $d = 3.0$  mm from each other on a Gaussian beam with an  $1/e^2$  waist of  $2w_b = 5.0$  mm and a spherical mirror of 5 cm focal length (see Section 4.B).
2. Using a mask with two slits of dimensions 1 cm  $\times$  100  $\mu\text{m}$  in a distance of 3 mm from each other (see Section 4.C).
3. Using a beam splitter (Si-wedge) for the wavefront splitting of the incoming beam into two parts. In order to make them converge and intersect, we use a mirror of  $f = 100$  cm focal length (see Section 4.D).

To meaningfully compare the three alternative configurations, we assume that in all three cases an XUV power  $\mathcal{P}_{\text{XUV}}$  is available and estimate the mean intensity that this power can produce in the interaction volume for each case. Subsequently, we obtain a *Figure of Merit*  $\mathcal{F}$  as the ratio of the mean intensity achieved at the focal region in each of the arrangements to a reference intensity  $\mathcal{I}_0$ . We choose as reference intensity the one obtained by the spherical mirror assumed in the two-aperture and two-slit arrangements but without any mask.

For a Gaussian beam profile, the intensity variation along the  $z$  axis of propagation and in the transverse  $r$  plane is  $\mathcal{I}(r, z) = (2\mathcal{P}_{\text{XUV}}/\pi w^2(z)) \exp[-(2r^2/w^2(z))]$ . Here  $w(z) \approx \theta_0 z$  is the waist radius far from focus and  $2w_0 = (2\lambda/\pi\theta_0)$  the focal spot size. The angle of convergence is estimated from  $\theta_0 \approx \arctan(w_b/f)$  where  $w_b = w(z=f) = \sqrt{2/\ln 2} r_b$  with  $r_b$  the initial beam radius and  $f$  the focal length of the spherical mirror. The focal mean intensity is easily seen to be  $\mathcal{I}_0 = (\mathcal{P}_{\text{XUV}}/\pi w_0^2)$ . We now estimate  $\mathcal{F}$  for each of the concrete cases (a) to (c).

(a) At the position of the apertures the intensity is reduced and therefore the power transmitted through each pinhole is

$$\mathcal{P}_{\text{apt}} = \mathcal{I}(d/2, f) \frac{\pi D^2}{4} = \frac{2\mathcal{P}_{\text{XUV}}}{\pi w_b^2} \exp\left(-\frac{d^2}{2w_b^2}\right) \frac{\pi D^2}{4}. \quad (18)$$

Given the small dimensions of the aperture, a flat-top distribution can be assumed, which gives rise to an Airy pattern at the focus. The radius of the central disk is then  $R_{\text{Airy}} \approx 1.22f\lambda_{q_0}/D \approx 54.2 \mu\text{m}$  with  $q_0 = 9$  the lowest harmonic in the selection. The mean intensity achieved in this case is then

$$\mathcal{I}_{\text{mean}} = 2 \frac{\mathcal{P}_{\text{apt}}}{\pi R_{\text{Airy}}^2}. \quad (19)$$

The corresponding figure of merit for the concrete example we have considered is  $\mathcal{F}_a = \mathcal{I}_{\text{mean}}/\mathcal{I}_0 \approx 8 \times 10^{-8}$ .

(b) The power through each slit with dimensions  $l_x = 1 \text{ cm}$  and  $l_y = 100 \mu\text{m}$  in this case is

$$\begin{aligned} \mathcal{P}_{\text{slit}} &\approx \frac{2\mathcal{P}_{\text{XUV}}}{\pi w_b^2} \exp\left(-\frac{d^2}{2w_b^2}\right) l_y \int_{-l_x/2}^{+l_x/2} \exp\left(-\frac{2x^2}{w_b^2}\right) dx \\ &\approx \frac{2\mathcal{P}_{\text{XUV}}}{\pi w_b^2} \exp\left(-\frac{d^2}{2w_b^2}\right) l_y \sqrt{\frac{\pi}{2}} w_b. \end{aligned} \quad (20)$$

The pattern at the focus will be elliptical with approximate dimensions  $L_x \approx 2 \cdot 1.22f\lambda_{q_0}/l_x \approx 1.1 \mu\text{m}$  and  $L_y \approx 2 \cdot 1.22f\lambda_{q_0}/l_y \approx 108.0 \mu\text{m}$ . Thus the mean intensity at focus follows as

$$\mathcal{I}_{\text{mean}} = 2 \frac{\mathcal{P}_{\text{slit}}}{L_x L_y}. \quad (21)$$

As expected, the figure of merit for the two-slit arrangement increases greatly and is found to be  $\mathcal{F}_b \approx 2.5 \times 10^{-4}$ .

(c) In the case of the beam splitter, the only difference from using the whole beam is the splitting of the Gaussian profile into two halves. A rough estimate of the mean intensity at focus from each half can be made using the same arguments as in case (b). The power from each half with dimensions  $l_x \approx w_b$

and  $l_y \approx w_b/2$  in this case is simply  $\mathcal{P}_{\text{XUV}}/2$ . Accordingly, the mean intensity at focus is

$$\mathcal{I}_{\text{mean}} = \frac{\mathcal{P}_{\text{XUV}}}{L_x L_y}. \quad (22)$$

As previously discussed in Section 4.D, the pattern at the focus will be elliptical with approximate dimensions  $L_x \approx 2f\lambda_{q_0}/(\pi l_x) \approx 22.2 \mu\text{m}$  and  $L_y \approx 2f\lambda_{q_0}/(\pi l_y) \approx 44.2 \mu\text{m}$  for  $f = 100 \text{ cm}$  and  $q_0 = 9$ . The corresponding FWHM values of the elliptical spot  $2r_{0,x} \approx 13.1 \mu\text{m}$  and  $2r_{0,y} \approx 26.2 \mu\text{m}$  are very close to the exact numerical results for the focal spot of H9 shown in Fig. 8. The figure of merit for the beam-splitter arrangement is, as expected, the highest  $\mathcal{F}_c \approx 1.0 \times 10^{-3}$ .

In case (c), we have not included the reflection losses on the intervening beam splitter. For relative low-order harmonics, the diagram in Fig. 7(c) indicates that they can be quite low. However, in a realistic case, one should consider a loss factor of up to 10, especially if the group of harmonics is comprised of high orders. These losses nevertheless are also present in the other setups as for most of the applications a stage for the suppression of the IR light is required. In this arrangement, the necessity of having long focal length to encompass at least three attoseconds in the focus results in lower XUV intensity, in the specific example by a factor of 400, but this is compensated by the large apertures (half the XUV beam profile) used. This makes the beam splitter most efficient, and in addition the sampling area of the XUV beam profile is more representative of the whole beam in this case.

## B. Parameter Selection

From the previous discussion in Section 5.A, it becomes apparent that one of the most efficient setups is the beam-splitter arrangement. Given the maximum resolution  $\Delta s$  associated with the ion microscope, there are two important parameters that will have to be appropriately chosen. They are the angle  $\theta$  at which the beams intersect each other and the focal length  $f$  of the focusing mirror. The angle  $\theta$  determines the distance  $a$  between the attosecond beats [see Eq. (1)], whereas the focal length defines the focal spot size and therefore the number of attosecond beats it encompasses. To illustrate this interplay, we have used Eqs. (10) and (11) to calculate the first- and second-order AC for a number of combinations of  $f$  and  $\theta$  values. Instead of assuming flat-top intensity profiles at the source, we have assumed Gaussian intensity distribution. This results in replacing the Bessel function in Eqs. (10) and (11) with a Gaussian function having the same argument. The rest of the parameters are the same as in the example shown in Fig. 8 except that for simplicity two complete Gaussian beams are assumed instead of two halves. The results are shown in Fig. 9 along with the modification of the signal assuming a spatial resolution of  $\Delta s = 2 \mu\text{m}$ .

There are two distinct substructures in the first- and second-order signals. The finer modulation represents the oscillations resulting from the superposition of the harmonic waves while the coarser is due to the beating of these waves giving rise to spatial localization i.e., to the formation of attosecond pulses. It is seen that under finite resolution conditions, the substructure in the first-order signal disappears to a large extent where, for the second-order signal the substructure after the convolution with the instrument function

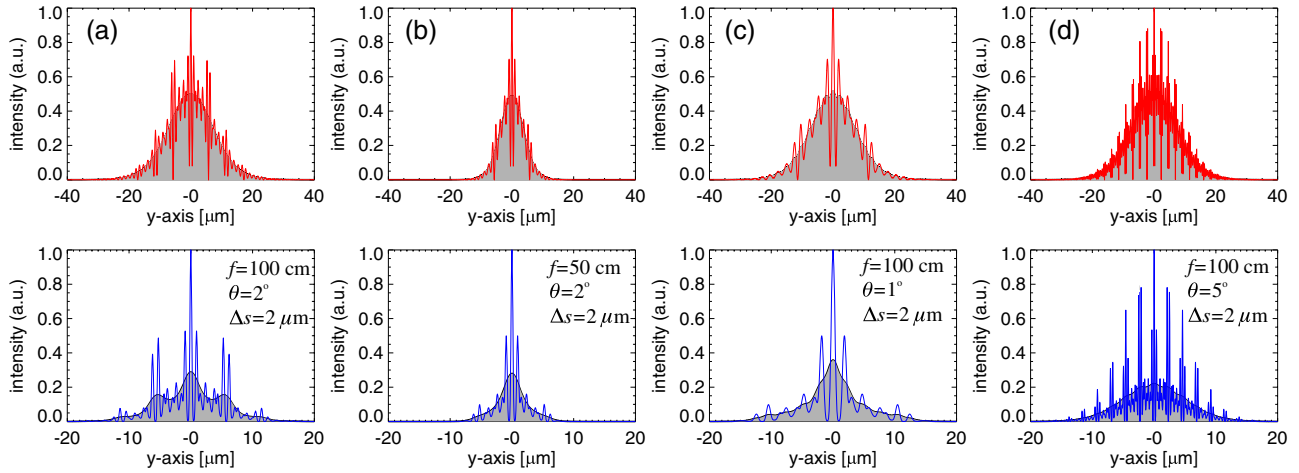


Fig. 9. Numerical calculation of the cross-beam arrangement using a wavefront beam splitter for the indicated combinations of focal lengths  $f$  and angles of intersection  $\theta$ . The upper panel shows the first-order AC trace while the lower the second-order. The apparent signal assuming a spatial resolution of  $\Delta s = 2 \mu\text{m}$  is shown as a gray shaded area.

prevails in most of the cases. For  $f = 100 \text{ cm}$  and  $\theta = 2^\circ$  three attosecond beats are contained in the focal spot as was also obtained by the numerical calculation shown in Fig. 8. The signal blurring due to finite resolution of the instrument is depicted by the gray shaded curve. In this case, the three attosecond peaks are still discernible, but the oscillations within the attosecond wave beating disappear, and the peak to background ratio is greatly reduced. Despite that, the duration of the peak in the middle of the second-order AC trace can be retrieved by careful deconvolution of the signal with the instrument function. For  $f = 50 \text{ cm}$  and  $\theta = 2^\circ$  the focal spot is half as large, and one cannot be sure whether the middle peak is affected by the focal spot size [see Fig. 9(b)]. For  $f = 100 \text{ cm}$  and  $\theta = 1^\circ$ , the middle peak is spread out to the point of seeing the oscillations within the attosecond beating, but the focal spot size cannot accommodate satellite peaks [see Fig. 9(c)]. This is required to verify the existence of a single attosecond pulse. In contrast, the case illustrated in Fig. 9(d), corresponding to  $f = 100 \text{ cm}$  and  $\theta = 5^\circ$ , exhibits a number of satellite peaks, but due to finite resolution they are smeared out and thus hardly discernible.

It is to be noted here that if the signal level allows it, a complete record of the second-order signal in the  $y$ - $z$  plane, such as the one shown in the lower panel of Fig. 8, can provide some of the most pertinent information even for finite resolution. A line-out of the signal along the axis of propagation of one of the beams contains the spatial characteristics of the beating structure and provides a substantial magnification. It is easily deduced that the modulation period of the attosecond beating in this case is  $a' = (\lambda_0/4)(1/\sin^2 \theta)$ , which for small angles  $\theta$  is considerably larger than the one given by Eq. (1). As the instrument resolution is the same over the whole field of view, such a projection might provide a clearer picture of the information sought after, e.g., whether a single or multiple as-pulses are present. This is depicted in Fig. 10 where the case studied in Section 4.D using the beam splitter is shown smoothed to a degree corresponding to  $\Delta s = 2 \mu\text{m}$ . It is seen that a line-out along the axis of propagation of one of the beams exhibits the multiple as-pulse structure. Clearly, it furnishes no additional information compared to a line-out perpendicular to the  $z$  axis but provides considerable magnification.

### C. Ionization Estimates

In order to establish to what extent the ion microscope described at length in [30] can record details of the focal region, we calculate the ion signal expected for a given peak intensity in the interaction region. We consider the case of the Si-wedge beam splitter discussed in Section 4.D and assume an XUV source delivering an intensity distribution at the overlap region of the form  $\mathcal{I}_{\text{XUV}}(\vec{r}, t) = \exp(-t^2/\tau_{\text{as}}^2)\mathcal{I}_{\text{peak}}F(\vec{r})$ . Here  $\tau_{\text{as}}$  is the duration of a single attosecond beat in the train delivered by the source and  $\mathcal{I}_{\text{peak}}F(\vec{r})$  is the spatial intensity distribution in the overlap region where  $\mathcal{I}_{\text{peak}}$  denotes the peak intensity available. We consider the specific example again, i.e., a harmonic composition consisting of the 9th to 15th harmonic a Ti:sapphire laser frequency ( $\lambda_L = 800 \text{ nm}$ ) and Helium gas as a two-photon ionization medium [33]. In general, the method is limited to photon energies in the range between IP/2 and IP of the ionization medium. The reason is that for lower photon energies, two-photon ionization is not occurring and, for higher photon energies, single-photon ionization will distort the measurement. Low photon energies do not present a problem because choosing Xenon as ionization medium, the fifth harmonic would already two-photon ionize it. For higher photon energies, direct double-ionization processes or direct ionization to higher charge states of the atom can be employed instead of single ionization. This is possible for short pulse durations [19].

The number of ions  $N_{\text{ions}}$  per shot for an attosecond pulse train comprising  $N_{\text{as}}$  attosecond pulses via two-photon ionization is estimated as

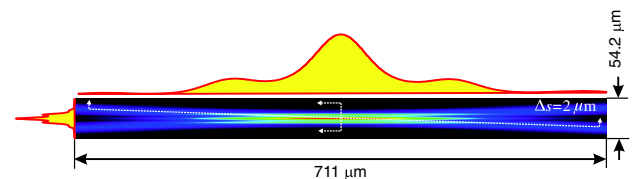


Fig. 10. Analysis of the 2D image of the beam-splitter case described in Section 4.D for an instrument resolution of  $\Delta s = 2 \mu\text{m}$ . The image has been smoothed to a degree corresponding to the finite instrument resolution and scaled to actual proportions. The line-outs along the axis of propagation of one of the beams and transverse to the  $z$  axis are shown by the red yellow-filled line.

**Table 1. Estimated Number of Ions for a Range of XUV Intensity Values and He Densities**

| $\mathcal{I}_{\text{peak}}$ [W/cm <sup>2</sup> ] | $\rho_{\text{He}}$ [ $\times 10^{18}$ cm <sup>-3</sup> ] | $N_{\text{ions}}$ |
|--|--|-------------------|
| 10 <sup>11</sup>                                 | 1.2  | 1                 |
|  | 6.2  | 7                 |
| 10 <sup>12</sup>                                 | 1.2  | 130               |
|  | 6.2  | 650               |
| 10 <sup>13</sup>                                 | 1.2  | $1.3 \times 10^4$ |
|  | 6.2  | $6.5 \times 10^4$ |

$$\begin{aligned}
N_{\text{ions}} &= N_{\text{as}} \times \sigma_{\text{He}}^{(2)} \times \int_{-\infty}^{+\infty} \int_V \rho_{\text{He}} \left( \frac{\mathcal{I}_{\text{XUV}}(\vec{r}, t)}{\hbar\omega_{\text{XUV}}} \right)^2 dt dV \\
&= N_{\text{as}} \times \sigma_{\text{He}}^{(2)} \times \rho_{\text{He}} \times \left[ \frac{\mathcal{I}_{\text{peak}}}{\hbar\omega_{\text{XUV}}} \right]^2 \int_{-\infty}^{+\infty} e^{-\frac{2t^2}{\tau_{\text{as}}^2}} dt \int_V F(\vec{r})^2 dV \\
&= N_{\text{as}} \times \sigma_{\text{He}}^{(2)} \times \rho_{\text{He}} \times \left[ \frac{\mathcal{I}_{\text{peak}}}{\hbar\omega_{\text{XUV}}} \right]^2 \sqrt{\frac{\pi}{2}} \times \tau_{\text{as}} \times F_V. \quad (23)
\end{aligned}$$

The spatial integral  $F_V = \int_V F(\vec{r})^2 dV \approx 3.7 \times 10^{-9}$  cm<sup>3</sup> is obtained numerically from the time-averaged intensity squared distribution given in the bottom row of Fig. 8. The cross-section for two-photon ionization of He for a mean photon energy of  $\hbar\omega_{\text{XUV}} \sim 20$  eV is in the literature given as  $\sigma_{\text{He}}^{(2)} \sim 10^{-52}$  cm<sup>4</sup> s [34]. Furthermore, we consider an He atom density in the range of  $\rho_{\text{He}} \approx (-16) \times 10^{18}$  cm<sup>-3</sup> corresponding to a pressure of 50–250 mbar. As it has already been mentioned for a train formed by the H9–H15 phase-locked harmonics of equal amplitude, the duration of the individual attosecond pulses is  $\tau_{\text{as}} \simeq 230$  as, and we assume a train of  $N_{\text{as}} = 10$  such attosecond pulses. Using Eq. (23), we have calculated the number of ions  $N_{\text{ions}}$  for an XUV source providing a peak intensity in the autocorrelation volume indicated in the first column of Table 1 and for two values of He ion concentrations.

It is seen that, while for  $\mathcal{I}_{\text{peak}} \approx 10^{11}$  W/cm<sup>2</sup> the expected number of ions is in the range of  $N_{\text{ions}} \lesssim 10$ , the number increases quadratically with intensity to the level of 10,000

for  $\mathcal{I}_{\text{peak}} \approx 10^{13}$  W/cm<sup>2</sup>. The signal due to this number of ions should be readily detectable by the ion microscope described in [30] at least for  $\mathcal{I}_{\text{peak}} \gtrsim 10^{12}$  W/cm<sup>2</sup>.

In view of the “graininess” of the signal due to a limited number of ions, and assuming a finite spatial resolution of the instrument, the question that arises is what is the minimum XUV intensity that would allow the retrieval of a statistically relevant signal from a single acquisition. To assess this, we have distributed the total number of ions  $N_{\text{ions}}$  in our estimation along the  $y$  axis according to the amplitude of the smoothed second-order signal in Fig. 8. This presumes that the XUV intensity along the  $z$  axis within the recorded area is approximately constant thus allowing binning along the same direction. The number of bins along the  $y$  axis is determined by the spatial resolution of the instrument. Assuming that the field of view of the ion microscope is approximately the same as the one indicated in the lower row of Fig. 8, there will be  $N_{\text{bin}} \sim 27$  bins for  $\Delta s = 2$   $\mu\text{m}$  and  $N_{\text{bin}} \sim 54$  bins for  $\Delta s = 1$   $\mu\text{m}$ . Let the average number of ions in the  $j$ th bin be  $\langle \Delta N_{\text{ion}}(j) \rangle$  normalized as to give  $\sum_j \langle \Delta N_{\text{ion}}(j) \rangle = N_{\text{ions}}$ . We now assume that in a single recording the number of ions in each of the bins are Poisson distributed with expected value (mean) equal to  $m = \langle \Delta N_{\text{ion}}(j) \rangle$ . Random deviates drawn from a Poisson distribution with that mean would then represent the fluctuations of the number of ions in each bin for a given total number of ions produced. Figure 11 depicts a simulated signal due to the expected fluctuations for a range of ion number and two instrument resolutions. It becomes apparent that for  $N_{\text{ions}} = 50$ , the signal recorded is not “clean” enough to reveal the information needed, as the fluctuations are too high and mask the details. The situation becomes considerably better for  $N_{\text{ions}} = 500$  while for  $N_{\text{ions}} = 1000$  a true reproduction of the second-order signal is expected even for  $\Delta s = 1$   $\mu\text{m}$ . Under these circumstances, one can assess the presence of a single attosecond pulse and estimate its duration. The mean value of the number of ions per bin is  $\sim N_{\text{ions}}/N_{\text{bin}}$ . Therefore, according to the Poisson distribution

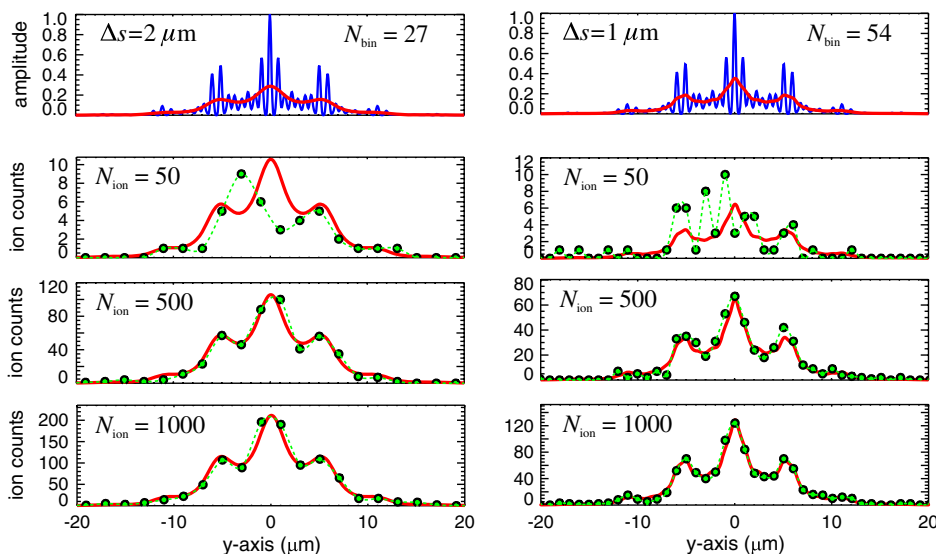


Fig. 11. Simulated ion signal for the indicated total number of ions and two different values of spatial resolution. The top row shows a line-out of the time-averaged second-order signal of the setup shown in Fig. 8 for infinite resolution (blue line) and convolved with the instrument function for finite resolution (red line) of  $\Delta s = 2$   $\mu\text{m}$  (left column) and  $\Delta s = 1$   $\mu\text{m}$  (right column). Assuming Poisson distribution for the number of ions in each bin, the statistical signal expected for the total number of ions indicated and the two resolution values are shown in the lower six panels by the green-filled points. The green dashed curve is a spline interpolation to guide the eye.

**Table 2. Summary of the Performance for the Three Setups Considered<sup>a</sup>**

| Setup                         | Characteristic Dimensions   | $f$ [cm] | $\mathcal{F}$  | Interaction Volume Dimensions (Second Order) [ $\mu\text{m}$ ] | Mean Intensity at Focus [ $\text{W}/\text{cm}^2$ ] | Number of Ions |
|-------------------------------|---|----------|----------------|--|--|----------------|
| Case (a)<br>Two-aperture mask | $D = 100 \mu\text{m}$<br>$d = 3 \text{ mm}$                           | 5        | $\sim 10^{-7}$ | $L_x \sim 28$<br>$L_y \sim 35$<br>$L_z \sim 1350$              | $\sim 10^8$  | $\sim 0$       |
| Case (b)<br>Two-slit mask     | $l_x = 100 \mu\text{m}$<br>$l_y = 5 \text{ mm}$<br>$d = 3 \text{ mm}$ | 5        | $\sim 10^{-4}$ | $L_x \sim 1$<br>$L_y \sim 30$<br>$L_z \sim 35$                 | $\sim 10^{11}$                                     | $\sim 6$       |
| Case (c)<br>Beam splitter     | $\theta = 2^\circ$  | 100      | $\sim 10^{-3}$ | $L_x \sim 10$<br>$L_y \sim 20$<br>$L_z \sim 400$               | $\sim 10^{12}$                                     | $\sim 650$     |

<sup>a</sup>The reference intensity assumed here is  $\mathcal{I}_0 = 10^{15} \text{ W}/\text{cm}^2$ . The dimensions of the interaction volume have been inferred from the calculated intensity distribution for each case. The number of ions is calculated according to the procedure outlined in Section 5.C for an He density of  $\rho_{\text{He}} = 6.2 \times 10^{18} \text{ cm}^{-3}$ . The symbols are defined in the text.

properties, the corresponding standard deviation is  $\sigma = \sqrt{m}$ ; thus the fluctuations in each bin scale with the total number of ions and bins as  $\delta N_{\text{ions}} \sim \sqrt{N_{\text{bin}}/N_{\text{ions}}}$  (see Fig. 11).

## 6. SUMMARY

In this report, we propose a novel approach to the metrology of attosecond pulses that requires only a single event record. The principle of a single-shot autocorrelator is based on the same idea as in the case of visible or infrared light, but it is designed to be used with XUV radiation. The objective is to be able to characterize the output of attosecond pulse sources in a convenient and reproducible way. We have analyzed and investigated the advantages and disadvantages of three different configurations and provided a comparative study. The main parameters associated with each of these setups are summarized in Table 2. In our estimates, we have come to the conclusion that a peak XUV intensity of  $\mathcal{I}_{\text{peak}} \approx 10^{12} \text{ W}/\text{cm}^2$  in the interaction region will be sufficient to provide an analyzable signal even in a single recording. This implies that the XUV source should deliver enough power, which when focused by a spherical mirror with  $f = 5 \text{ cm}$  would produce a peak intensity of  $\mathcal{I}_{\text{peak}} \approx 10^{15} \text{ W}/\text{cm}^2$ . This intensity level appears quite within reach [17, 19]. The XUV energy needed to produce this intensity with a train of 10 as-pulses and for ideal focusing conditions is estimated to be 30 nJ. Although the concept appears feasible and within reach, there are a number of practical problems that will have to be addressed before it can be routinely used. To identify these problems, an experiment has to be performed with a source of XUV light providing enough intensity to ionize an atomic medium in a two-photon process.

## ACKNOWLEDGMENTS

This work was funded in part by the European Commission programs ATTOFEL, CRISP, Laserlab Europe, the Greek funding program NSRF, and by the Association EURATOM-MPI für Plasmaphysik. It was performed in the framework of the DAAD-IKYDA program for the promotion of scientific cooperation between Greece and Germany (project number 51128343). We would like to thank Guangjin Ma for converting the code written by one of us (GDT) to FORTRAN90 language, thus reducing considerably the computing time. We also thank Matthew Weidman for reading the manuscript and making useful suggestions.

## REFERENCES

1. M. Hentschel, R. Kienberger, Ch. Spielmann, G. A. Reider, N. Milosevic, T. Brabec, P. Corkum, U. Heinzmann, M. Drescher, and F. Krausz, "Attosecond metrology," *Nature* **414**, 509–513 (2001).
2. A. Baltuska, Th. Udem, M. Uiberacker, M. Hentschel, E. Goulielmakis, Ch. Gohle, R. Holzwarth, V. S. Yakovlev, A. Scrinzi, T. W. Hänsch, and F. Krausz, "Attosecond control of electronic processes by intense light fields," *Nature* **421**, 611–615 (2003).
3. F. Krausz and M. Ivanov, "Attosecond physics," *Rev. Mod. Phys.* **81**, 163–234 (2009).
4. F. Quéré, J. Itatani, G. L. Yudin, and P. B. Corkum, "Temporal characterization of attosecond pulses," in *Ultrafast Optics IV*, F. Krausz, G. Korn, P. Corkum, and I. A. Walmsley, eds. Vol. **95** of Springer Series in Optical Sciences (Springer, 2004), pp. 259–270.
5. P. M. Paul, E. S. Toma, P. Breger, G. Mullot, F. Augé, Ph. Balcou, H. G. Muller, and P. Agostini, "Observation of a train of attosecond pulses from high harmonic generation," *Science* **292**, 1689–1692 (2001).
6. H. G. Muller, "Reconstruction of attosecond harmonic beating by interference of two-photon transitions," *Appl. Phys. B* **74**, s17–s21 (2002).
7. Y. Mairesse, A. de Bohan, L. J. Frasinski, H. Merdji, L. C. Dinu, P. Monchicourt, P. Breger, M. Kovacev, R. Taeb, B. Carré, H. G. Muller, P. Agostini, and P. Salières, "Attosecond synchronization of high-harmonic soft x-rays," *Science* **302**, 1540–1543 (2003).
8. Y. Mairesse and F. Quéré, "Frequency-resolved optical gating for complete reconstruction of attosecond bursts," *Phys. Rev. A* **71**, 011401 (2005).
9. M. Drescher, M. Hentschel, R. Kienberger, G. Tempea, C. Spielmann, G. A. Reider, P. B. Corkum, and F. Krausz, "X-ray pulses approaching the attosecond frontier," *Science* **291**, 1923–1927 (2001).
10. R. Kienberger, E. Goulielmakis, M. Uiberacker, A. Baltuska, V. Yakovlev, F. Bammer, A. Scrinzi, Th. Westerwalbesloh, U. Kleineberg, U. Heinzmann, M. Drescher, and F. Krausz, "Atomic transient recorder," *Nature* **427**, 817–821 (2004).
11. E. Goulielmakis, M. Uiberacker, R. Kienberger, A. Baltuska, V. Yakovlev, A. Scrinzi, Th. Westerwalbesloh, U. Kleineberg, U. Heinzmann, M. Drescher, and F. Krausz, "Direct measurement of light waves," *Science* **305**, 1267–1269 (2004).
12. J. Gagnon, E. Goulielmakis, and V. S. Yakovlev, "The accurate FROG characterization of attosecond pulses from streaking measurements," *Appl. Phys. B* **92**, 25–32 (2008).
13. Y. Kobayashi, T. Sekikawa, Y. Nabekawa, and S. Watanabe, "27-fs extreme ultraviolet pulse generation by high-order harmonics," *Opt. Lett.* **23**, 64–66 (1998).
14. P. Tzallas, D. Charalambidis, N. A. Papadogiannis, K. Witte, and G. D. Tsakiris, "Direct observation of attosecond light bunching," *Nature* **426**, 267–271 (2003).
15. Y. Nabekawa, T. Shimizu, T. Okino, K. Furusawa, H. Hasegawa, K. Yamanouchi, and K. Midorikawa, "Conclusive evidence of an attosecond pulse train observed with the mode-resolved

- autocorrelation technique,” *Phys. Rev. Lett.* **96**, 083901 (2006).
16. Y. Nomura, R. Hörlein, P. Tzallas, B. Dromey, S. Rykovanov, Zs. Major, J. Osterhoff, S. Karsch, L. Veisz, M. Zepf, D. Charalambidis, F. Krausz, and G. D. Tsakiris, “Attosecond phase-locking of harmonics emitted from laser-produced plasmas,” *Nat. Phys.* **5**, 124–128 (2008).
  17. Y. Nabekawa, T. Shimizu, T. Okino, K. Furusawa, H. Hasegawa, K. Yamanouchi, and K. Midorikawa, “Interferometric autocorrelation of an attosecond pulse train in the single-cycle regime,” *Phys. Rev. Lett.* **97**, 153904 (2006).
  18. P. Heissler, P. Tzallas, J. M. Mikhailova, K. Khrennikov, L. Waldecker, F. Krausz, S. Karsch, D. Charalambidis, and G. D. Tsakiris, “Two-photon above-threshold ionization using extreme-ultraviolet harmonic emission from relativistic laser-plasma interaction,” *New J. Phys.* **14**, 043025 (2012).
  19. P. Tzallas, E. Skantzakis, L. A. A. Nikolopoulos, G. D. Tsakiris, and D. Charalambidis, “Extreme-ultraviolet pump-probe studies of one-femtosecond-scale electron dynamics,” *Nat. Phys.* **7**, 781–784 (2011).
  20. K. Midorikawa, Y. Nabekawa, and A. Suda, “XUV multiphoton processes with intense high-order harmonics,” *Prog. Quantum Electron.* **32**, 43–88 (2008).
  21. P. A. Carpeggiani, P. Tzallas, A. Palacios, D. Gray, F. Martín, and D. Charalambidis, “Disclosing intrinsic molecular dynamics on the 1-fs scale through extreme-ultraviolet pump-probe measurements,” *Phys. Rev. A* **89**, 023420 (2014).
  22. I. Grguras, A. R. Maier, C. Behrens, T. Mazza, T. J. Kelly, P. Radcliffe, S. Dusterer, A. K. Kazansky, N. M. Kabachnik, Th. Tschentscher, J. T. Costello, M. Meyer, M. C. Hoffmann, H. Schlarb, and A. L. Cavalieri, “Ultrafast x-ray pulse characterization at free-electron lasers,” *Nat. Photonics* **6**, 852–857 (2012).
  23. Y. Mairesse, O. Gobert, P. Breger, H. Merdji, P. Meynadier, P. Monchicourt, M. Perdrix, P. Salières, and B. Carré, “High harmonic XUV spectral phase interferometry for direct electric-field reconstruction,” *Phys. Rev. Lett.* **94**, 173903 (2005).
  24. E. Cormier, I. A. Walmsley, E. M. Kosik, A. S. Wyatt, L. Corner, and L. F. DiMauro, “Self-referencing, spectrally, or spatially encoded spectral interferometry for the complete characterization of attosecond electromagnetic pulses,” *Phys. Rev. Lett.* **94**, 033905 (2005).
  25. J. Janszky, G. Corradi, and R. N. Gyuzalian, “On a possibility of analysing the temporal characteristics of short light pulses,” *Opt. Commun.* **23**, 293–298 (1977).
  26. F. Salin, P. Georges, G. Roger, and A. Brun, “Single-shot measurement of a 52-fs pulse,” *Appl. Opt.* **26**, 4528–4531 (1987).
  27. P. Simon, H. Gerhardt, and S. Szatmari, “A single-shot autocorrelator for UV femtosecond pulses,” *Meas. Sci. Technol.* **1**, 637–639 (1990).
  28. A. Brun, P. Georges, G. Le Saux, and F. Salin, “Single-shot characterization of ultrashort light pulses,” *J. Phys. D* **24**, 1225–1233 (1991).
  29. L. A. A. Nikolopoulos, E. P. Benis, P. Tzallas, D. Charalambidis, K. Witte, and G. D. Tsakiris, “Second order autocorrelation of an XUV attosecond pulse train,” *Phys. Rev. Lett.* **94**, 113905 (2005).
  30. M. Schultze, B. Bergues, H. Schröder, F. Krausz, and K. L. Kompa, “Spatially resolved measurement of ionization yields in the focus of an intense laser pulse,” *New J. Phys.* **13**, 033001 (2011).
  31. P. Heissler, R. Hörlein, J. M. Mikhailova, L. Waldecker, P. Tzallas, A. Buck, K. Schmid, C. M. S. Sears, F. Krausz, L. Veisz, M. Zepf, and G. D. Tsakiris, “Few-cycle driven relativistically oscillating plasma mirrors: a source of intense isolated attosecond pulses,” *Phys. Rev. Lett.* **108**, 235003 (2012).
  32. M. Born and E. Wolf, *Principles of Optics* (Pergamon, 1985).
  33. N. A. Papadogiannis, L. A. A. Nikolopoulos, D. Charalambidis, G. D. Tsakiris, P. Tzallas, and K. Witte, “On the feasibility of performing non-linear autocorrelation with attosecond pulse trains,” *Appl. Phys. B* **76**, 721–727 (2003).
  34. A. Saenz and P. Lambropoulos, “Theoretical two- three- and four-photon ionization cross sections of helium in the XUV range,” *J. Phys. B* **32**, 5629–5637 (1999).